A carbon-doped tantalum dioxyfluoride as a superior electron transport material for high performance organic optoelectronics

Vasilopoulou, M., Mohd Yusoff, A. R. B., Kuganathan, N., Bao, X., Verykios, A., Polydorou, E., Armadorou, K-K., Soultati, A., Papadimitropoulos, G., Irfan Haider, M., Fakharuddin, A., C. Palilis, L., Kennou, S., Chroneos, A., Argitis, P. & Davazogloua, D.

Original citation & hyperlink:
Vasilopoulou, M, Mohd Yusoff, ARB, Kuganathan, N, Bao, X, Verykios, A, Polydorou, E, Armadorou, K-K, Soultati, A, Papadimitropoulos, G, Irfan Haider, M, Fakharuddin, A, C. Palilis, L, Kennou, S, Chroneos, A, Argitis, P & Davazogloua, D 2020, 'A carbon-doped tantalum dioxyfluoride as a superior electron transport material for high performance organic optoelectronics', Nano Energy, vol. 70, 104508.
https://dx.doi.org/10.1016/j.nanoen.2020.104508

DOI 10.1016/j.nanoen.2020.104508
ISSN 2211-2855

Publisher: Elsevier

Carbon-doped tantalum dioxyfluoride with superior electron transport properties for organic optoelectronics

Maria Vasilopoulou,[1,] Kuganathan Navaratnarajah,[2,3] Xichang Bao,[4] Abd Rashid Bin Mohd Yusoff,[5] Anastasia Soultati,[1] Georgios Papadimitropoulos,[1] Azhar Fakharuddin,[6,7] Muhammad Irfan Haider,[6,8] Stella Kennou,[9] Panagiotis Argitis,[1] Alexander Chroneos,[2] Dimitris Davazoglou[1]*

[1]Institute of Nanoscience and Nanotechnology (INN), National Center for Scientific Research (NCSR) "Demokritos", 15341 Agia Paraskevi, Attica, Greece

[2]Department of Materials, Imperial College London, London SW7 2AZ, UK

[3]Faculty of Engineering, Environment and Computing, Coventry University, Priory Street, Coventry CV1 5FB, United Kingdom

[4]Qingdao Institute of Bioenergy and Bioprocess Technology, Chinese Academy of Sciences, Qingdao 266101, China

[5]Advanced Display Research Center, Department of Information Display, Kyung Hee University, 130-701 Seoul, South Korea.

[6]Department of Physics, University of Konstanz, 78457 Konstanz, Germany

[7]IMEC Kapeldreef 75, Heverlee 3001, Belgium (present affiliation)

[8]Department of Chemistry, Quaid-i-Azam University, Islamabad 45320, Pakistan

[9]Department of Chemical Engineering, University of Patras, 26504 Patras, Greece

*Corresponding author: MV (m.vasilopoulou@inn.demokritos.gr)

Abstract

The design and development of functional materials with superior electron transport capabilities is the key to advances in the field of optoelectronic devices. Earth-abundant transition metal oxyhalide and carbon-doped semiconductors have been investigated as electrode materials in catalytic devices owing to their exceptional physical properties, high electrical conductivity, excellent robustness and enhanced chemical stability. However, there are no reports so far about their potential application in other optoelectronic devices such as light emitting diodes and solar cells. Here, we designed and developed by adopting a simple preparation process a ternary compound namely a carbon-doped tantalum dioxyfluoride (TaO_2FC_x) and explored its effectiveness as an electron transport material in organic optoelectronic devices. By combining excellent n-type conductivity, high transparency, defect-free electronic structure, low refractive index, enhanced hydrophobicity and robustness, the newly developed ternary compound was proven an outstanding electron transport material in both organic light emitting diodes and solar cells of diverse architectures delivering higher efficiencies compared to well-established electron transport layers and, thus, extending its potential as a highly promising material for solid state lighting and solar energy production.

There is a growing consensus that optoelectronic devices using solution-processed semiconductors such as organic semiconductors and organic-inorganic perovskites will play a central role in the near future applications in solid state lighting and solar

energy exploration because of their low cost and enhanced performance.[1,2] Solution-processable organic optoelectronic devices such as organic light emitting diodes (OLEDs) and organic solar cells (OSCs) although they lag behind in efficiency compared to their perovskite counterparts they continue to draw large interest due to their higher stability and non-toxicity.[3,4] Furthermore, the academic community has recently witnessed an unprecedented evolution in their performance characteristics implying they will soon become mature technologies for industrial applications. This has been mainly accomplished by the development of novel semiconductors such as non-fullerene acceptors and more advanced device architectures.[5-9] However, further improvements in the efficiency characteristics of OLEDs and OSCs and, most importantly, in operational and long-term temporal stabilities are vital for their widespread use and commercialization.

A critical aspect for enhanced device performance is the carrier injection/transport efficiency of the electrodes to/from the (photo)active organic materials. In particular, the electron transport layer is indispensable for achieving high electron transfer rates to/from the cathode electrode and maximize the device efficiency.[10,11] Except for appropriate energy levels in order to form a type II (i.e. staggered gap) heterojunction with the organic semiconductor, an ideal electron transport layer (ETL) should also possess an adequate n-type conductivity, a low refractive index to enhance the out-coupling efficiency, robustness and a high hydrophobicity and overall environmental stability to restrict water adsorption on the organic semiconductor surface and prolong the device stability.[12,13]Especially, in devices with forward (i.e. p-i-n) architecture the latter is highly crucial in order to avoid moisture's penetration into the active organic layer prior to the cathode deposition. To date, various types of electron transport materials, such as alkali-earth metals,[14] polyamine compounds,[15,16]

polyelectrolytes,[17,18] poly(ionic liquids),[19,20] and metal salts and bases,[21,22] have been developed. Remarkably, research on the intrinsically robust and environmental stable inorganic transition-metal oxides for application as ETLs in organic and related perovskite optoelectronics is scarce, with the highly defective zinc oxide (ZnO) and titanium dioxide (TiO_2) and the less-defective tin oxide (SnO_2) to be the only metal oxides reported so far.[23-26] To bring the organic and related optoelectronics in a more mature level for technological applications, a significant advancement in the metal oxide based charge transport interlayers is urgently needed.

Tantalum pentoxide (Ta_2O_5), a non-defective wide bandgap material with a large refractive index possessing high thermal and chemical stability under various environments, has attracted significant attention as a high dielectric constant gate oxide for applications in field-effect transistors (FETs) and resistive memories as well as in the coating and photocatalytic fields.[27,28] However, its' very large optical band gap (higher than 4.0 eV) and extremely low electrical conductivity render stoichiometric Ta_2O_5 highly unsuitable as either hole or electron transport material for applications, such as solar energy to electricity conversion and solid state lighting. Recently, Y. Wan et al. reported a tantalum sub-oxide (TaO_x) as a robust electron selective heterocontact for crystalline silicon photovoltaics and photo-electrochemical water reduction.[29] Moreover, tantalum oxynitride (TaON),[30] tantalum dioxychloride (TaO_2Cl),[31] and dioxyfluoride (TaO_2F),[32] and the MXene family member tantalum carbide (TaC),[33] have been recently considered as excellent electrocatalysts to several catalytic reactions due to their suitable optical bandgap and superior charge transfer rates. Among them, TaO_2F has been considered as the most stable inorganic compound in nature as it exhibits the highest known melting points of all materials.[32,34] Moreover, carbon-doped tantalum oxide was proven beneficial for memory applications whereas

TaC can reach nearly metallic conductivity.[33] Motivated by the above research work, we designed and developed a novel ternary compound with exceptional optoelectronic properties, in particular, a carbon-doped tantalum dioxyfluoride (TaO_2FC_x) that exhibits a combination of energy levels perfectly matched with those of most organic semiconductors, high electron conductivity, extremely low refractive index and high hydrophobicity, therefore representing an ideal choice for the cathode interface of several types of OLEDs and OSCs.

Fig. 1a illustrates the preparation process of the ternary compound. Tantalum oxide vapors produced by heating a superficially oxidized tantalum (Ta) filament reacted with hexafluoroacetone (C_3F_6O) vapors introduced inside the deposition chamber by bubbling of a nitrogen (N_2) stream through a saturator kept at 60 ^oC. The ternary material was deposited to form thin films on top of selected substrates which remained at room temperature. X-ray (XPS) and ultra-violet (UPS) photoelectron spectroscopy was employed to reveal the atomic composition (i.e.stoichiometry), valence band and work function of the material, which are critical to its application as electron selective layer. Fig. 1b depicts the Ta 4f XPS core levels; they consist of two different doublet peaks attributed to Ta $4f_{7/2}$ and Ta $4f_{5/2}$. In the first doublet the Ta $4f_{7/2}$ peaks at 26.2 and is attributed to the stoichiometric oxide phase.[35] The second doublet is shifted to higher energies and the Ta $4f_{7/2}$ appears at 26.9 eV.[36] This doublet is assigned to a fluorinated oxide phase and the shift to higher energies is due to the high electronegativity of fluorine anion.[37] The F 1s spectrum (Fig. 1c) can be fitted with two Gaussian components peaked at 688.1 and 684.8 eV attributed to fluorine anions bonded to Ta and C, respectively.[38,39] This indicates the incorporation of C within the structure of the developed material. The O 1s spectrum (Fig. 1d) is also fitted with two Gaussian components one positioned at 530.8 and attributed to

Ta-O bonds, and a second peaked at 531.9 eV attributed to -OH groups due to surface contamination. From the XPS analysis a material's stoichiometry of TaO_2FC_x is evident.

Fig. 1e depicts the high binding energy cut-off region (left), the full valence band (middle) and the near Fermi level region (right) of the UPS spectrum of TaO_2FC_x. The valence band maximum (VBM) appears at 3.0 eV below the Fermi level whereas the work function (W_F) is estimated at 4.3 eV. No defect band appears inside the band gap, suggesting that the synthesized material is non-defective. It also has a lower bandgap than the pristine tantalum pentoxide we deposited in an oxygen environment (Supplementary Figs. 1a and 2a, Supporting Information) whereas it is highly transparent in the visible (Supplementary Fig. 1b) which is highly desirable when applied at the bottom cathode electrode of inverted devices. In the X-ray diffraction pattern of the deposited material (Fig. 1f), three crystalline peaks appear at 2θ positions of 33º, 62º and 65º. These peaks are characteristic of tantalum oxyfluoride,[40,41] while those at 33º and 65º could also be related to the formation of Ta_2C phase.[42,43] Note that, the Ta oxide deposited without the injection of hexafluoroacetone appears completely amorphous (Fig. S3). Additionally, the materials exhibited a very low refractive index of about 1.3 in the visible and near-IR region (Fig. 1g) which is attributed to its high fluorine content.[44] The refractive index of the pristine oxide was about 2.0 (Fig. S4) in accordance with the literature.[45] The surface topography of the ternary compound is grain-like (Fig. 1h) with the grain size, thickness and surface roughness to be easily controlled by changing the deposition environment and time (Fig. S5). Those changes had no significant impact on the materials stoichiometry (Figs. S6 and S8), thus offering a window to optimize our processing/deposition conditions. The high fluorine content also resulted in an

increased hydrophobicity of the synthesized material (inset, Fig. 1g), especially when compared to the pristine oxide (Fig. S2b); this is highly beneficial for application as a buffer layer for moisture in organic and related optoelectronics. The developed material also exhibited an n-type conductivity of 1.26 S cm^{-1} (Fig. 1i) whereas the pristine oxide was insulating (Fig. 1i), as expected.[46]

Theoretical calculations were also performed to shed more light on the properties of the developed material. The bulk structure of TaO_2F belongs to the cubic crystal system with the space group of $Pm\bar{3}m$.[47] Crystallographic refinement of O/F ratio on the shared site exhibits a value of 0.6667:0.3333 implying a disordered composition (partially occupied) but maintaining stoichiometry. Before we examine the electronic structure and binding energies of a single gaseous carbon atom trapped in a TaO_2F lattice, it was necessary to consider a full occupancy model without modifying the overall composition. Three possible models (Fig. S7) were identified. The lattice energies of three structures were compared by performing geometry optimizations (both ion positions and cell parameters). Simulations find that all three structures have similar energies suggesting that all three structures are identical. In order to consider the most favorable scenario of an interstitial C atom in the non-defective structure **I,** a 3×3×3 supercell consisting of 108 atoms was generated. Fig. S8 shows the relaxed supercell structure and its density of states plot (DOS). Calculations reveal that bulk TaO_2F has a band gap of ~3.0 eV. Various possible interstitial positions were considered and four promising relaxed structures were identified. Geometry optimized structures together with a view of C interstitials are shown in Fig. S10.

In the first configuration (**P**), C is in the centre of the cubic motif without forming significant bonds with oxygen or fluorine (Fig. S9). This is reflected in the calculated bond distances and the almost zero Bader charge. There is a small distortion in the

lattice. Binding energy is –0.60 eV suggesting that the C in this interstitial position is more stable than its isolated gaseous atom. Interstitial C introduces a peak at the top of the valence band without altering the band gap, making this material non-defective as also indicated by UPS. Charge density around C is shown in Fig. 2. The second configuration (**Q**) consists of an interstitial C along the *bc* plane with a significant interaction with oxygen and fluorine (Supplementary Table 1 and Fig. S9) reflecting in the Bader charge and relatively short bond distances. The interstitial C becomes slightly positive. The attractive interaction between C and O is slightly stronger compared to that of F according to the bond distances.[48] The binding energy of C for the formation of this configuration is –0.20 eV, less favorable that of configuration **P**. Howevwe, there is a significant binding in the configuration **R**. In this configuration, C forms four short bonds with oxygens lie on the *ac* plane. On the other handfluorine is further away from C and its interaction with C is weak as observed in the C-F distances. Binding energy is –1.15 eV more exoergic than that observed in **P** and **Q**. The strong binding is reflected in the Bader charge (slightly more positive than that noted in **P** and **Q**) and charge density around the C and its neighboring atoms (Fig. 2). The fourth configuration (**S**) exhibits the strongest interaction between C and O in the lattice. The binding energy is –5.89 eV meaning that there is a significant interaction with the lattice. Fig. S10 shows the strong bonding interaction between C and oxygen. This is reflected in the shortest C-O bond distance (1.29 Å). Moreover, there is a distortion in the lattice with F atoms moving slightly further away. DOS and atomic DOS plots clearly show that the peak introduced by the C is now mixed with the valence band. Strong bonding interaction is also reflected in the charge density plot.

We next deposited a TaO_2FC_x film with an approximate thickness of 6 nm (Fig. S11) on top of the green-emissive organic semiconductor poly[(9,9-dioctylfluorenyl-2,7-

diyl)-co-(1,4-benzo-2,1′,3-thiadiazole)] (F8BT) and evaluated its electron injection/transport capability. The alteration of the surface topography of F8BT (Fig. S12) and the detection of Ta 4f XPS peaks on F8BT (Fig. S13) indicated the successful deposition of the ternary compound on top of F8BT. The forward OLED configuration (Fig. S14) consisted of an indium tin oxide (ITO) layer as the transparent bottom anode electrode, a poly(3,4-ethylenedioxythiophene) polystyrene sulfonate (PEDOT-PSS) film with a thickness of 40 nm as the hole transport layer (HTL), the emissive layer (F8BT or the blue emitting poly[2-(6-cyano- 6'-methylheptyloxy)-1,4- phenylene] (CN-PPP)) and the top aluminum cathode. In the reference devices a commonly used cesium carbonate (Cs_2CO_3) film was served as ETL for comparison. Fig. S15 presents the schematic energy level diagram of the materials used in the OLED structure considering vacuum level alignment before contact. The valence (VB) and conduction band (CB) edges of TaO_2FC_x were estimated from UPS and absorption measurements whereas the energy levels of the other OLED materials were taken from the literature.[49] The estimated CB value of 3.95(±0.1) eV for TaO_2FC_x is expected to be highly beneficial for electron transport as it is located between the lowest unoccupied molecular orbital (LUMO) of the emissive layers and the Al cathode work function thus forming a type II heterojunction with F8BT. Fig. 3a presents the current density-voltage-luminance (J-V-L) characteristics of the F8BT-based OLEDs. Fig. 3b, Fig. S16 and Fig. 3c show the current, power and external electroluminescence (EL) quantum efficiency of OLEDs versus the current density. Supplementary Table S2 summarizes the OLEDs performance characteristics which are highly improved when incorporating TaO_2FC_x as the ETL instead of Cs_2CO_3.[50] The C-doped Ta dioxyfluoride-modified device exhibited an ultra-low turn-on voltage (2.0 eV) that is even lower than the F8BT's

bandgap (Fig. S17) indicating a highly improved electron injection. This was also proven by the J-V characteristics of electron-only devices (Fig. S18). The achieved current efficiency of 16.53 cd/A is among the highest ever reported for OLEDs using thin (about 100 nm) F8BT emissive layers.[51,52] The EL spectra were very similar to the photoluminescence (PL) emission spectrum of F8BT (Figs 3d and Fig. S17a) suggesting that EL emission originates from excitons generated exclusively inside F8BT. Note that the hybrid oxide worked as an effective ETL also in blue OLEDs (Fig. S19) based on the CN-PPP emitter having a higher LUMO level than F8BT. As one of the major issues in OLEDs is their operational stability, this was investigated for both (reference and TaO_2FC_x-modified) F8BT-based OLEDs. It is observed that whereas the reference device retained lower than 60% of its initial luminance after 100 h of constant operation under a 15 mA cm^{-2} current density (Figs. 3e, 3f), the device with the C-doped Ta dioxyfluoride ETL retained above 90% of its initial luminance due to the superior quality of the modified cathode interface and the capability to act as a protective layer due to its high robustness and hydrophobicity. UPS measurements taken on a F8BT film prior to (Fig. S20) and after the deposition of TaO_2FC_x on top of it (Fig. 3g) revealed a remarkable decrease in the electron injection barrier from 1.1 (Fig. 3h) to 0.3 eV (Fig. 3i) which explains the superiority of the ternary compound as an electron injection/transport layer. Such a large reduction in the electron injection barrier can be directly related to enhanced electron injection/transport rates towards the emissive layer and overall improvement of the quality of the cathode interface as injection barriers 0-0.3 eV indicate the formation of an Ohmic rather than a Schottky contact.[53]

To explore the potential for universal application of the developed material in other organic optoelectronic devices, we fabricated single junction binary OSCs with the

forward architecture based on blends of conjugated polymer donors with both fullerene (Poly[4,8-bis(5-(2-ethylhexyl)thiophen-2-yl)benzo[1,2-*b*;4,5-*b'*]dithiophene-2,6-diyl-*alt*-(4-(2-ethylhexyl)-3-fluorothieno[3,4-*b*]thiophene-)-(2-carboxylate-2-6-diyl)]: phenyl-C_{71}-butyric acid methyl ester, PTB7-Th:$PC_{71}BM$) and non-fullerene (poly[(2,6-(4,8-bis(5-(2-ethylhexyl-3-fluoro)thiophen-2-yl)-benzo[1,2-b:4,5-b']dithiophene))-alt-(5,5-(1',3'-di-2-thienyl-5',7'-bis(2-ethylhexyl)benzo[1',2'-c:4',5'-c']dithiophene-4,8-dione)]:3,9-bis(2-methylene-((3-(1,1-dicyanomethylene)-6,7-difluoro)-indanone))-5,5,11,11-tetrakis(4-hexylphenyl)-dithieno[2,3-d:2',3'-d']-s-indaceno[1,2-b:5,6-b']dithiophene, MP6:IT-4F) acceptors (Fig. S21). The control devices included the well-established perylene diimide amino N-oxide (PDINO) as ETL on top of the photoactive blend. For the PTB7-Th:$PC_{71}BM$ based OSCs, a significant improvement in power conversion efficiency (PCE) up to 10.31% was obtained in the TaO_2FC_x-modified device compared to the reference device with the PDINO (PCE up to 9.40%) (Fig. S22 and Supplementary Table 3). The enhanced OSC performance can be assigned to the high quality of the cathode contact as indicated by the lower bimolecular recombination (Fig. S23) and improved electron transport in the photoactive blend (Fig. S24 and Supplementary Table 4) of the TaO_2FC_x based device. Added to the merits is the high long-term stability of the "self-encapsulated" TaO_2FC_x modified devices which is directly related to the robustness and hydrophobic nature of the ternary material. The appropriate position of the CB edge of TaO_2FC_x facilitates electron extraction from the LUMO of $PC_{71}BM$ (~ 3.9 eV) and the LUMOs of the recently developed non-fullerene acceptors (~ 4.0 eV) (Fig. 4a) towards Al by acting as an intermediate energy step. As a result, the MP6:IT-4F based OSC with a forward architecture ITO/PEDOT-PSS/MP6:IT-4F/ETL/Al and the TaO_2FC_x as ETL reached a high maximum PCE of 13.18% (Fig.

4b and Supplementary Table 5) and an average PCE of 12.77% (Fig. 4c), thus representing a significant enhancement relative to the control device with PDINO (PCE_{max}=12.04%). The enhanced photon-to-electron conversion efficiency (Fig. 4d) and improved electron transport (Fig. 4e and Supplementary Table 6 with the calculated electron mobilities) revealed the high quality of the cathode interface in this device configuration. The incorporation of TaO_2FC_x also contributed to the excellent device long-term stability when exposed to ambient conditions (Fig. 4f). Importantly, a large improvement in performance was also obtained in OSCs with the inverted architecture FTO/ETL (40 nm)/MP6:IT-4F/MoO_x/Al using either our developed material or the widely used ZnO as the bottom ETL. The control device showed an inferior performance (reaching a maximum PCE of 12.10%) compared to the TaO_2FC_x one (PCE_{max}=13.82%) due to the advantages of the ternary material discussed above. This represents one of the higher efficiencies of single junction PM6:IT-4F based OSCs reported to date.[54,55] Additionally, the higher UV-Vis absorption of the PM6:IT-4F film on top of TaO_2FC_x (Fig. S25) is assigned to the higher transmittance (lower absorption) of the cathode contact, the absence of trap states on the surface of the ternary compound (Fig. S26) and an improved nanomorphology of the photoactive layer due to the higher hydrophobicity of the TaO_2FC_x compared to ZnO (Fig. S27). All these observations verify the superior role of the C-doped Ta dioxyfluoride as an advanced electron transport material and open a new era for the application of non-defective oxide-based materials in optoelectronic devices.

In summary, we have developed an efficient electron transport material for optoelectronic applications through a simple and low-cost deposition method. As a result, fluorescent green OLEDs with current efficiencies of 16.53 cd/A and non-

fullerene OSCs reaching PCEs of 13.82 % were demonstrated with the additional advantage of high operational and temporal stability. Our methodology of TaO_2FC_x preparation could easily be extended to other simple and well-established deposition techniques including solution-processing to enable the low-cost development of carbon-doped metal oxyfluoride semiconductors that may open new avenues and create opportunities for research not only in organic but also in silicon, perovskite and quantum-dot solar cells and light emitting devices.

Methods

Preparation of C-doped tantalum dioxifluoride. Carbon-doped tantalum dioxyfluoride films were deposited in a MOCVD reactor using tantalum oxide and hexafluoroacetone (purchased from Sigma-Aldrich) vapors. Tantalum oxide vapors were produced by heating a superficially oxidized metallic (Ta) filament (purchased from Merck) at a temperature of 1000 ^oC. The hexafluoroacetone vapor was introduced in the deposition chamber by bubbling of a (10 sccm) N_2 stream through a saturator kept at 60 ^oC. For the deposition, substrates were loaded on a copper susceptor located 5 cm below the filament, which was fixed between two Cu current leads. The chamber was subsequently evacuated to 10^{-2} Torr and the gases (100 sccm of N_2 and hexafluoroacetone vapors) were introduced. Then, the pressure was automatically stabilized to 1 Torr with the aid of a pressure control system comprising a baratron manometer and a butterfly valve. After stabilization of flows and pressure, the filament was heated with the application of an AC (50 Hz) current. Bias voltage and deposition time was used to control the film thickness and the times used varied between 1 second and 60 seconds. The deposition of a pristine Ta oxide was

performed in oxygen environment without the introduction of hexafluoroacetone vapors inside the chamber. During deposition the substrate remained near room temperature.

Theoretical methodology. All calculations were performed using dispersion corrected density functional theory (DFT+D) as implemented in the VASP code, which solves the standard Kohn-Sham equations using plane wave basis sets. For the exchange correlation energy term the Generalised Gradient Approximation (GGA) has been used in the form of the PBEsol functional. The standard projected augmented wave (PAW) potentials and a plane-wave basis set with a cut off value of 500 eV were employed. A 4×2×4 Monkhorst,- k point mesh, which yielded 20 k points was used in all calculations. The valence electronic configurations for Ta, O and F were $5p^6 6s^2 5d^3$, $2s^2 2p^4$ and $2s^2 2p^5$. Structural optimizations were performed using a conjugate gradient algorithm and the forces on the atoms were obtained from the Hellmann-Feynman theorem including Pulay corrections. In all optimized structures, forces on the atoms were smaller than 0.001 eV/Å. In this work, dispersion has been included by using the pair-wise force field as implemented by Grimme *et al*. in the VASP package.

OLED device preparation. OLED devices were fabricated on ITO coated glass substrates (sheet resistance of 20 Ω/sq) which served as anode bottom electrodes. Prior to the deposition of organic semiconductors, the substrates were successivelysonicated for 10 min in acetone, 2-propanol and DI water and then dried in nitrogen flow. Next, the substrates were subjected to oxygen plasma treatment for 10 minutes followed by deposition of a thin (~40 nm) layer of poly(3,4-ethylenedioxythiophene)-poly(styrenesulfonate) (PEDOT-PSS, 1.3 wt. % dispersion

in H_2O) (purchased from Sigma Aldrich) which was filtered using a 0.45μm PVDF filter and spin coated in ambient conditions at 7000 rpm for 40 sec and then annealed at 130 ^oC for 30 min. The emissive layer (F8BT, with a 9:1 F8:BT ratio, purchased from American Dyes Source, ADS 233 YE) was then spin coated from a 10 mg mL^{-1} solution in chloroform (filtered through a 0.22 μm pore size PTFE filter) at 1200 rpm for 40 sec to form a ~ 100 nm thick layer on top of PEDOT-PSS and then annealed at 95 ^oC for 10 min. In the control devices, a thin Cs_2CO_3 layer was deposited on top of F8BT via spin coating (at 2000 rpm for 40 sec) from a methanol solution with a concentration of 5 mg mL^{-1} to serve as electron injection/transport layer. For the deposition of tantalum dioxyfluoride some devices were transferred in a dedicated deposition chamber. The devices were finally completed with a 150 nm aluminum cathode deposited through a shadow mask in a dedicated chamber.

OSC device fabrication. OSCs with the forward architecture were fabricated on PEDOT-PSS deposited on pre-cleaned ITO/glass substrates. The substrates were subsequently transferred in an argon filled glove box for the deposition of the photoactive layer. The MP6F:IT-4F (both purchased from Ossila) blend was dissolved in chlorobenzene (CB) solvent at the concentration of 20 mg/ml (1:1 ratio) and stirred at 40°C for 3h. Before spin coating, 1,8-iodooctane (DIO) (0.6%, v/v) was added to the solution. The films were spin coated at 1700 rpm for 60 s and then thermally treated at 100 ^oC for 10 min. The photoactive PTB7-Th:$PC_{71}BM$ blend (both purchased from Ossila) was dissolved in 1,2 dichlorobenzene (*o*-DCB) at the concentration of 25 mg/ml (1:1.5 ratio) and stirred at 60 ^oC for 3 h. Prior to spin-coating DIO (3%, v/v) was added to the solution. The films were spin coated inside an argon filled glove box at 1000 rpm for 90 sec and left to dry without any thermal treatment. The control samples were thenmodified with a PDINO film that was spin

coated from a 5 mg/ml solution in methanol at 2000 rpm for 40 s without any other treatment whereas the samples with carbon-doped tantalum dioxyfluoride were immediately transferred from the glove box to the dedicated deposition camber. The fabrication procedure was completed upon the deposition of the Al top electrode in a thermal evaporator using shadow masks to define the active area. For the OSCs with the inverted architecture, a 30 nm thick ETL was deposited on pre-cleaned and O_2 plasma treated FTO substrates. ZnO layers were prepared by spin-coating 0.5 mol/L zinc acetate dihydrate in ethanolamine and 2-methoxyethanol which were then heated at 200 ^oC for 30 min. The TaO_2FC_x layer was deposited as described above followed by the deposition of the MP6:IT-4F blend and of 10nm thick MoO_x capped with a 150 nm Al anode. The device active area was 0.13 cm^2.

Electron mobilities calculation. To model current space charge limited conduction (SCLC) and obtain the electron mobility of the MP6:IT-4F and PTB7-Th:$PC_{71}BM$ blend in electron-only devices, the measured current-voltage data were fitted in the SCLC regime to Mott-Gurney's law, including the Frenkel effect on the electric field dependent mobility, given by the following equation:

$$J = (9/8)\varepsilon_0\varepsilon_r\mu_0 \exp[0{,}89\beta\{(V/d\}^{1/2}](V^2)/(d^3), \quad \text{(equation S1)}$$

for current density J, applied voltage V, permittivity of free space ε_0, relative permittivity of the blend ε_r (e_r=3.5), zero-field electron mobility μ_0, field activation factor β and active layer thickness d (d=120 nm). The fitting parameters μ_0 and β are listed in Tables S1 and S2, respectively, and were calculated from the intercept and slope of the J vs. $V^{1/2}$ plot.

Photoelectron spectroscopy. XPS and UPS measurements characterized the surface chemical composition and the electronic structure of TaO_2FC_x films deposited either

on ITO/glass or on an F8BT substrate. All samples were measured as fabricated, without cleaning or any other treatment before introducing them into the ultra-high vacuum chamber. An unmonochromatized Mg Ka line at 1253.6 eV (12 keV with 15 mA anode current) and an analyser (Leybold EA-11) pass energy of 100 eV, giving a full width at half maximum, FWHM, of 1.3 eV for the Au $4f_{7/2}$ peak, were used for the XPS measurements whereas the XPS analysis was carried out at 0 degrees take-off angle. In all XPS spectra the BE of the predominant aliphatic contribution to the C 1s peak at 284.8 eV was used as a measured BE reference. The analysed area was approximately a 2×5 mm^2 rectangle positioned near the geometric centre of each sample. The UPS measurements (that was taken first followed by XPS measurements) were performed using the He I (21.2eV) excitation line and a voltage of 12.23V that was applied to the specimen in order to separate the high BE cut-off from the analyser.

X-Ray diffraction measurements. The crystal structure of TaO_2FC_x films (on silicon) was studied by recording the XRD patterns with a Siemens D-500 diffractometer operating with Cu radiation in Bragg-Brentano geometry. Structural refinements were performed with the Rietveld method using the Fullprof software.

Optical measurements. UV-Vis absorption/transmittance spectra were taken with a Perkin Elmer Lambda 40 UV/Vis spectrometer.

Surface topography measurements. Surface topographies were monitored with an NT-MDT atomic force microscope (AFM) operating in tapping mode and with a JEOL 7401f field emission scanning electron microscope (FESEM).

OLED characterization. J-V characteristics of OLEDs were measured with a Keithley 2400 source-measure unit. Luminance and electroluminescence (EL) spectra

were recorded with an Ocean Optics USB 2000 fiber optic spectrophotometer (assuming a Lambertian emission profile).

OSC characterization. For the J-V characteristics of OSCs taken under light illumination and in the dark, a Keithley 2400 source-measure unit and a solar simulator equipped with a Xe lamp and an AM 1.5G filter were used. The EQE spectra were collected with a Autolab PGSTAT-30 potentiostat using a 300 W Xe lamp and an Oriel 1/8 monochromator.

Acknowledgments

Author contributions

M.V., P.A. and D.D. designed the research. G.P. prepared TaO_2FC_x and conducted XRD, and SEM characterizations. K.N. and A.C. carried out the theoretical calculations. M.V., A.S., X.B. and A.R.B.M.Y conducted the device experiments. S.K. conducted the XPS, UPS measurements. M.V. and D.D. supervised the experimental work. M.V. wrote the manuscript with contributions from the other authors.

Competing interests

The authors declare no competing interests.

Additional information

Supplementary information is available for this paper.

References

1. Wang, Q. et al. Oxysulfide photocatalyst for visible-light-driven overall water splitting. *Nat. Mater.*, https://doi.org/10.1038/s41563-019-0399-z (2019).
2. Bala, C. R., Breen, S., Shao, Y., Ardo, S. & Weber, A. Z. Evaluating particle-suspension reactor designs for Z-scheme solar water splitting via transport and kinetic modeling. *Energy Environ. Sci.* **11**, 115–135 (2018).
3. Burroughes, J. H. et al. Light-emitting diodes based on conjugated polymers. *Nature* **347**, 539–541 (1990).
4. Forrest, S. R. The path to ubiquitous and low-cost organic electronic appliances on plastic. *Nature* **428**, 911–918, (**2004**).
5. He, Z. et al. Single-junction polymer solar cells with high efficiency and photovoltage. *Nat. Photonics* **9**, 174–179 (2015).
6. Li, G., Zhu, R. & Yang, Y. Polymer solar cells. *Nat. Photonics* **6**, 153–161 (2012).
7. Chueh, C.-C., Li, C.-Z. & Jen, A. K. Y. Recent progress and perspective in solution-processed interfacial materials for efficient and stable polymer and organometal perovskite solar cells. *Energy Environ. Sci.* **8**, 1160–1189 (2015).
8. Wang, F., Tan, Z. A. & Li, Y. Solution-processable metal oxides/chelates as electrode buffer layers for efficient and stable polymer solar cells. *Energy Environ. Sci.* **8**, 1059–1091 (2015).
9. Yin, Z., Wei, J. & Zheng, Q. Interfacial materials for organic solar cells: Recent advances and perspectives. *Adv. Sci.* **3**, 1500362 (2016).

10. Lai, T.-H., Tsang, S.-W., Manders, J. R., Chen, S. & So, F. Properties of interlayer for organic photovoltaics. *Mater. Today* **16**, 424–432 (2013).
11. Zhao, W. et al. Molecular optimization enables over 13% efficiency in organic solar cells. *J. Am. Chem. Soc.* **139**, 7148–7151 (2017).
12. Vasilopoulou, M. et al. Annealing-free highly crystalline solution-processed molecular metal oxides for efficient single-junction and tandem polymer solar cells. *Energy Environm. Sci.* **8**, 2448–2463 (2015).
13. Hovern, C. V. et al. Electron injection into organic semiconductor devices from high work function cathodes. *Proc. Natl. Acad. Sci. U.S.A* **105**, 12730–12735 (2008).
14. Murawski, C., Leo, K. & Gather. M. Efficiency roll-off in organic light-emitting diodes. *Adv. Mater.* **25**, 6801−6827 (2013).
15. Lee, B. R. et al. Amine-based interfacial molecules for inverted polymer-based optoelectronic devices. *Adv. Mater.* **27**, 3553–3559 (2015).
16. Lee, B. R. et al. Amine-based polar solvent treatment for highly efficient inverted polymer solar cells. *Adv. Mater.* **26,** 494−500 (2014).
17. Lee, B. H. et al. Multi-charged conjugated polyelectrolytes as a versatile work function modifier for organic electronic devices. *Adv. Funct. Mater.* **24**, 100–1108 (2014).
18. Hovern, C. et al. Ion motion in conjugated polyelectrolyte electron transporting layers. *J. Am. Chem. Soc.* **129**, 10976–10977 (2007).
19. Georgiadou, D. G. et al. Influence of the anion on the optoelectronic characteristics of triphenylsulfonium salts modified polymer light emitting devices. *Synth. Met.* **181**, 37–44 (2013).

20. Kim, T. Y. et al. Poly(3,4ethylenedioxythiophene) derived from poly(ionic liquid) for the use as hole-injecting material in organic light-emitting diodes. *Macromol. Rapid Comm.* **30**, 1477–1482 (2009).
21. Cooke, G., Evans, I. R. & Skabara, P. J. Functional organic materials for optoelectronic applications. *J. Mater. Chem. C* **7**, 6492–6492 (2019).
22. Lu, L. P., Kabra, D. & Friend, R. H. Barium hydroxide as an interlayer between zinc oxide and a luminescent conjugated polymer for light-emitting diodes. *Adv. Funct. Mater.* **22**, 4165–4171 (2012).
23. Lange, I. et al. Tuning the work function of polar zinc oxide surfaces using modified phosphonic acid self-assembled monolayers. *Adv. Funct. Mater.* **24**, 7014–7024 (2014).
24. Liu, M., Johnston, M. B. & Snaith, H. J. Efficient planar heterojunction perovskite solar cells by vapour deposition. *Nature* **501**, 395–398 (2013).
25. Zhou, H. et al. Interface engineering of highly efficient perovskite solar cells. *Science* **345**, 542−546 (2014).
26. Abuhelaiqa, M. et al. Stable perovskite solar cells using tin acetylacetonate based electron transporting layers. *Energy Environ. Sci.* **12**, 1910−1917 (2019).
27. Li, C., Wang, T., Luo, Z., Zhang, D. & Gong, J. Transparent ALD-grown Ta_2O_5 protective layer for highly stable ZnO photoelectrode in solar water splitting. *Chem. Commun.* **51**, 7290−7293 (2015).
28. Chen, S. & Wang, L.-W. Thermodynamic oxidation and reduction potentials of photocatalytic semiconductors in aqueous solution. *Chem. Mater.* **24**, 3659−3666 (2012).

29. Wan, Y. et al. Tantalum oxide electron-selective heterocontacts for silicon photovoltaics and photoelectrochemical water reduction. *ACS Energy Lett.* **31**, 125−131 (2018).

30. Nakamura, R., Tanaka, T. & Nakato, Y. Oxygen photoevolution on a tantalum oxynitride photocatalyst under visible-light irradiation: How does water photooxidation proceed on a metal−oxynitride Surface? *J. Phys. Chem. B* **109**, 8920−8927 (2005).

31. Tu, H., Xu, L., Mou, F. & Guan. J. Single crystalline tantalum oxychloride microcubes: controllable synthesis, formation mechanism and enhanced photocatalytic hydrogen production activity. *Chem. Commun.* **51**, 12455−12458 (2015).

32. Yue, X., Jin, Y. & Shen, P. K. Highly stable and efficient non-precious metal electrocatalysts of tantalum dioxyfluoride used for the oxygen evolution reaction. *J. Mater. Chem. A* **5**, 8287−8291 (2017).

33. Yue, X. et al. Fluorine-doped and partially oxidized tantalum carbides as nonprecious metal electrocatalysts for methanol oxidation reaction in acidic media. *Adv. Mater.* **28**, 2163–2169 (2016).

34. Antonelli, D. M. & Ying, J. Y. Synthesis and characterization of hexagonally packed mesoporous tantalum oxide molecular sieves. *Chem. Mater.* **8**, 874–881 (1996).

35. Abbas, Y. et al. Compliance-free, digital SET and analog RESET synaptic characteristics of sub-tantalum oxide based neuromorphic device. *Sci. Rep. 8*, 1228 (2018).

36. Xin, Y. & Shen, P. K. Tantalum carbide doped by fluorine as non-precious metal anodic electrocatalyst superior to Pt/C for glycerol-oxidation. *Electrochim. Acta* **227**, 267–274 (2017).

37. Simpson, R., White, R. G., Watts, J. F. & Baker, M. A. XPS investigation of monatomic and cluster argon ion sputtering of tantalum pentoxide. *Appl. Surf. Sci.* **405**, 79–87 (2017).

38. Horikawa, T. et al. Preparation of nitrogen-doped porous carbon by ammonia gas treatment and the effects of N-doping on water adsorption. *Carbon* **50**, 1833–1842 (2012).

39. Agulyansky, A. The Chemistry of Tantalum and Niobium Fluoride Compounds. 8–10 (Elsevier, Boston, 2004)

40. Frevel, L. K. & Rinn, H. W. The crystal structure of NbO_2F and TaO_2F, *Acta Crystallogr*. **9**, 626–627 (1956).

41. Gutman, V. & Jack, K. H. The crystal structures of molybdenum trifluoride, MoF_3, and tantalum trifluoride, TaF_3, *Acta Crystallogr*. **4**, 244–246 (1951).

42. Brar, L. K., Singla, G. & Pandey, O. P. Evolution of structural and thermal properties of carbon-coated TaC nanopowder synthesized by single step reduction of Ta-ethoxide. *RSC Adv.* **5**, 1406–1416 (2015) .

43. Fukunaga, A., Chu, F. & McHenry, M. E. Synthesis, structure, and superconducting properties of tantalum carbide nanorods and nanoparticles. *J. of Mater. Research* **13**(9), 2465–2471 (1998).

44. Biffinger, J. C. & Kim, H. W. The polar hydrophobicity of fluorinated compounds. *ChemBioChem* **5**, 622–627 (2004).

45. Hodgkinson, I., Wu, Q. h. & Hazel. J. Empirical equations for the principal refractive indices and column angle of obliquely deposited films of tantalum oxide, titanium oxide, and zirconium oxide. *Appl. Opt.* **37**, 2653–2659 (1993).

46. Liu, L. et al. Fluorine doping: a feasible solution to enhancing the conductivity of high-resistance wide bandgap $Mg_{0.51}Zn_{0.49}O$ active components, *Sci. Rep.* **5**, 15516 (2015).
47. Kresse, G. & Joubert, D. From ultrasoft pseudopotentials to the projector augmented-wave method. *Phys. Rev. B* **59**, 1758–1775 (1999).
48. Perdew, J. P. *et al*. Restoring the density-gradient expansion for exchange in solids and surfaces. *Phys. Rev. Lett.* **100**, 136406 (2008).
49. Georgiadou, D. G. et al. Effect of triphenylsulfonium triflate addition in wide band-gap polymer light emitting diodes: improved charge injection, transport and electroplex-induced emission tuning. *RSC Adv.* **2**, 11786–11792 (2012).
50. Zhao, J. et al. The role of cesium carbonate on the electron injection and transport enhancement in organic layer by admittance spectroscopy. *Appl. Phys. Lett.* **101**, 193303 (2012).
51. Lee, B. R. et al. Highly efficient inverted polymer light-emitting diodes using surface modifications of ZnO layer. *Nature Comm.* **5**, 4840 (2014).
52. Sessolo, M. & Bolink, H. J. Hybrid organic–inorganic light–emitting diodes. *Adv. Mater.* **23**, 1829–1845 (2011).
53. Vandewal, K. et al. Efficient charge generation by relaxed charge-transfer states at organic interfaces. *Nat. Mater.* **13**, 63–68 (2014).
54. Yuan, J. et al. Single-Junction Organic Solar Cell with over 15% Efficiency Using Fused-Ring Acceptor with Electron-Deficient Core. *Joule* **3**(4), 1140–1151 (2019).
55. Zhang, S. et al. Over 14% Efficiency in Polymer Solar Cells Enabled by a Chlorinated Polymer Donor. *Adv. Mater*. **30** (28), 1800613 (2018).

Figures

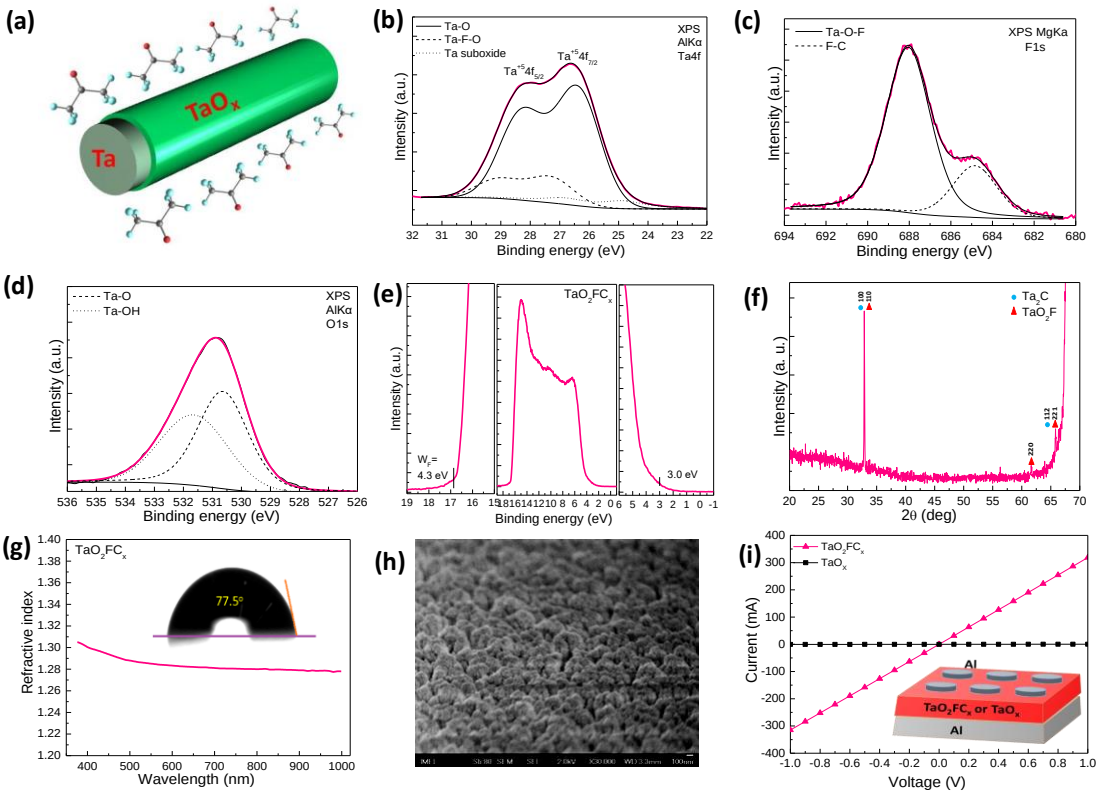

Figure 1 Structure, electronic and physical properties of TaO_2FC_x. a, Schematic illustration of the procedure for the synthesis of TaO_2FC_x. **b,** Ta 4f, **c,** F 1s and **d,** O 1s XPS peaks of the tantalum dioxylfluoride film deposited on ITO substrate. **e,** UPS spectrum of the same film. **f,** X-ray diffraction pattern, **g,** measured refractive index and **h,** SEM topography of the TaO_2FC_x film deposited on silicon substrate. The water contact angle measurement of this film is shown as inset in Fig. 1g. **i,** Current-voltage characteristics of the device with a structure $Al/TaO_2FC_x/Al$ (shown as inset). The respected characteristics of the structure $Al/TaO_x/Al$ is also shown for comparison.

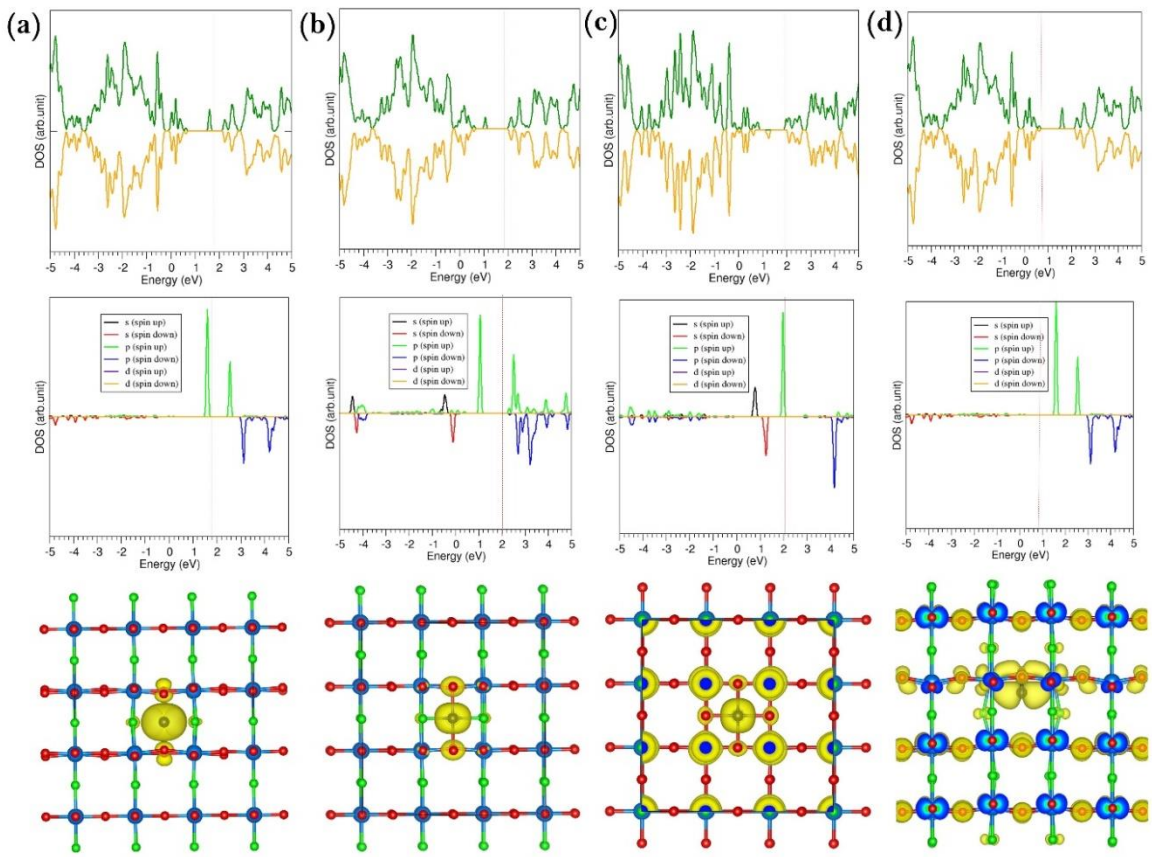

Figure 2 Theoretical calculations. Total DOS plots, Atomic DOS for C and constant charge density plots associated with C in the relaxed configurations. Plots **a, b, c,** and **d,** correspond to the configurations P, Q, R and S respectively.

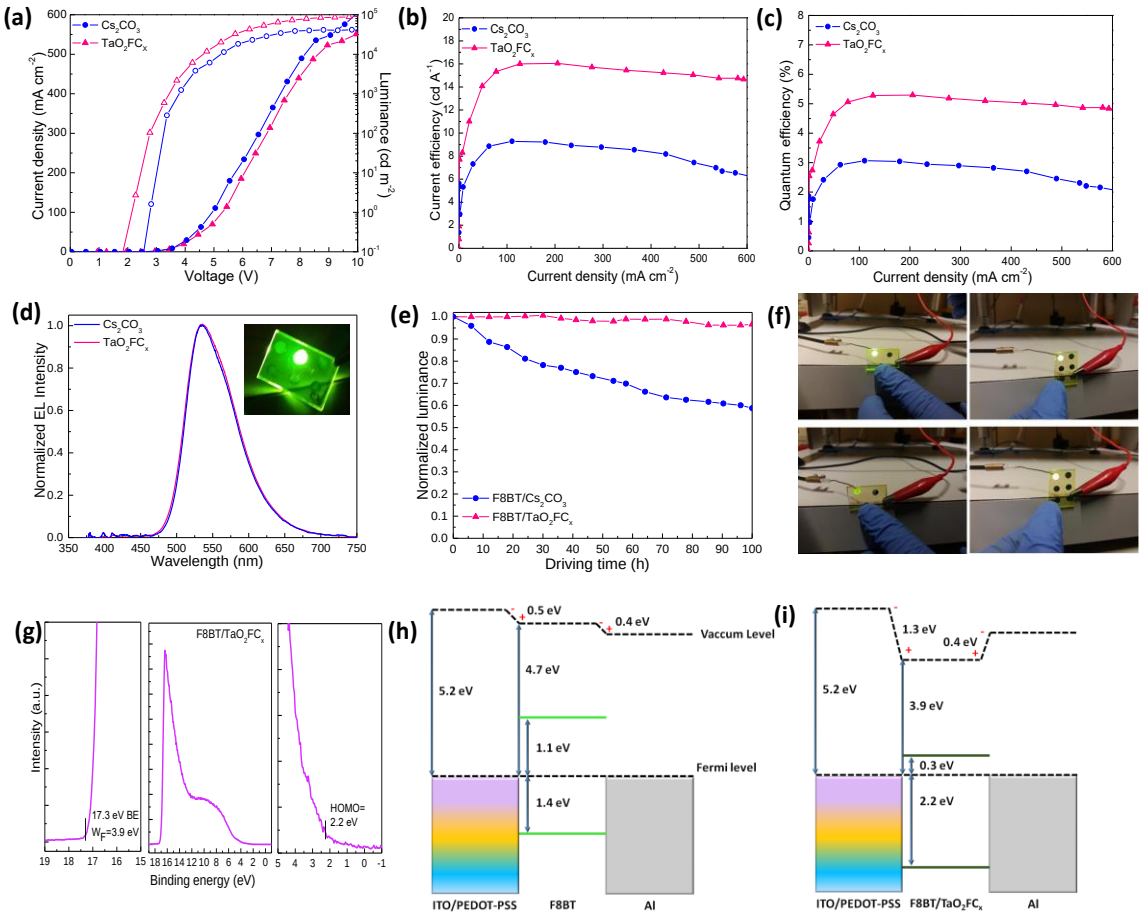

Figure 3 OLED device performance. **a,** Current density and luminance versus voltage (J−V−L) characteristics, **b,** current efficiency and **c,** external EL quantum efficiency versus current density of the F8BT-based OLEDs using either Ca_2CO_3 or TaO_2FC_x films as the electron transport layer. **d,** The EL spectra of the corresponding devices at an applied voltage of 6V. **e,** Lifetime measurements: Normalized luminance versus driving time of the F8BT-based OLEDs at a constant current density of 15 mA cm^{-2}. **f,** Photographs of the working OLEDs having Ca_2CO_3 (left) and TaO_2FC_x (right) as the electron selective contacts at 0 h (up) and 100 h (down) of constant operation. **g,** UPS spectra (left: the high binding energy cut-off, middle: an expanded view and right: the near Fermi level region) of an F8BT film deposited on PEDOT-PSS on ITO/glass substrate after the deposition of the TaO_2FC_x film. The corresponding energy level diagram of the OLED devices with the configuration **h,** ITO/PEDOT-PSS/F8BT/Al and **i,** ITO/PEDOT-PSS/F8BT/TaO_2FC_x/Al, assuming a constant Fermi level at thermodynamic equilibrium.

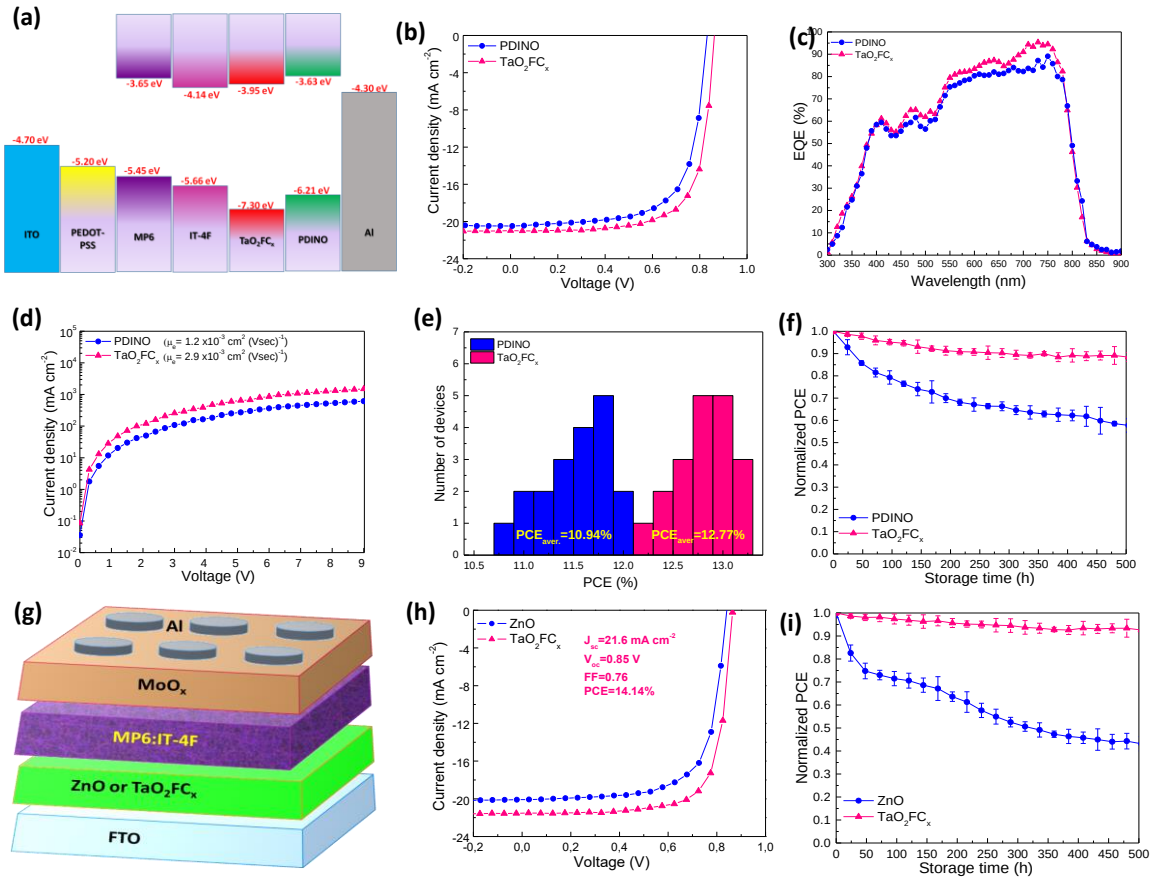

Figure 4 OSC device performance. a, The energy levels of the materials used in the MP6:IT-4F OSCs (before contact, considering vacuum level alignment). **b,** J-V characteristic curves taken under 1.5 AM illumination and **c,** EQE spectra of MP6:IT-4F based OSCs. **d,** The J-V characteristics of electron-only devices, **e,** the PCE statistics and **f,** variation of PCE versus storage time of unencapsulated devices. **g,** The inverted OSC architecture, **h,** J-V under 1.5 AM illumination of the devices shown in (g) and **i,** The variation of PCE of unencapsulated inverted devices versus storage time.